Semiclassical description of high-order-harmonic spectroscopy of the Cooper minimum in krypton

F. Cloux, B. Fabre, and B. Pons
CELIA, University of Bordeaux, CNRS UMR 5107, CEA, 351 Cours de la Libération, 33405 Talence, France
(Received 24 November 2014; published 12 February 2015)

The Cooper minimum has recently been observed in the high-order-harmonic spectrum issued from the interaction of a short and intense laser pulse with krypton atoms [A. D. Shiner *et al.*, J. Phys. B **45**, 074010 (2012)]. Here we compare this observation to a semiclassical description using the single-active electron approximation. Particular attention is paid to the description of the interaction of the active valence electron with the ionic core in the framework of a mean-field approach. The computed harmonic spectrum presents a minimum at about 83 eV, which does not show up so clearly in the measurements probably because of second-order diffraction of the grating used to disperse the harmonic spectrum.

DOI: 10.1103/PhysRevA.91.023415 PACS number(s): 32.80.Rm, 42.65.Ky

I. INTRODUCTION

Photoionization spectroscopy is an optical technique that has been developed to probe the structure of matter. It has been applied to a large set of atomic and molecular systems [1,2] and it has even been employed in condensed matter contexts [3]. Dynamical information on some photoinduced chemical reactions can also be deduced from photoionization experiments using pump-probe techniques (see, e.g., [4,5]). However, with the advent of short and intense laser pulses, a new technique, with improved spatial and temporal accuracies, has emerged: the so-called high-order-harmonic spectroscopy (HHS). High-harmonic generation (HHG) is suitably described in terms of a three-step process [6]: an electron is tunnel-ionized from the target under the influence of the strong field; it is then accelerated and driven back to the ionic target core as the field changes sign. Radiative recombination then occurs and results in the emission of a photon in the extreme ultraviolet spectral range. Within the last step, the returning electron probes the target as does the impinging photon in conventional photoionization. The energy of the returning electron can reach $3.17U_P$, where U_p is the ponderomotive energy of the laser pulse, which corresponds to large de Broglie wavelengths for typical infrared (intense) pulses. Moreover, HHG mainly occurs within an oscillation of the primary laser field. These two characteristics explain the improved accuracies of HHS, down to the Angström and attosecond scales [7], respectively. Furthermore, the geometrical properties of the target can be resolved more easily in HHG setups than in the usual photoionization; in the former case, the momentum vector of the scanning returning electron can be easily handled—by using an elliptical one-color field [8] or orthogonally polarized two-color fields [9]—while retrieving vectorial properties from photoelectron spectra necessitates rather complicated detection techniques of coincidences between ejected particles [11,12]. A large amount of work has thus been devoted to decoding from HHG spectra structural [9,10,13] and dynamical [14,15] information on atomic and molecular systems.

These experimental works have motivated theoretical investigations. However, it was soon realized that accurate modeling of HHS is very demanding, especially in the case of molecular targets. Multiple orbitals can contribute to the HHG signal [16], the holes created by primary tunnel ionization can evolve nonadiabatically [17], and the nuclear and electronic degrees of freedom can be effectively coupled [18,19]. The modeling is commonly thought to become easier for atomic targets, particularly for rare-gas species whose inner shells lie deeply in the energy scale so that they cannot be efficiently ionized and therefore would not participate in the HHG process (see, however, [20,21]). These "simple" atomic systems are thus appropriate candidates for characterizing in depth some fundamental capabilities of HHG spectroscopy, and this explains the recent revival of HHS experiments on rare-gas atoms [20,22–24]. In particular, the occurrence and characterization of the Cooper minimum in the HHG spectra of Ar have been the subject of many works [10,23–27]; Cooper minima are indeed direct traces of the target electronic structure [28] that HHS aims at picturing. In spite of some controversial observations about the importance of HHG phase matching [23,24], all experiments have demonstrated that the Cooper minimum clearly shows up in the HHG spectra of Ar. Simulations [26,27] have indicated that the precise location of the Cooper minimum within the HHG spectrum is significantly influenced by multichannel (multielectron) interactions, which is at variance with the common neglect of inner shell contributions. However, calculations performed in the framework of the single-active electron (SAE) approximation [29] and employing a carefully optimized model potential [30] reproduced the experimental findings [23]. Moreover, these semiclassical calculations, labeled CTMC-QUEST as they combine classical trajectory Monte Carlo (CTMC) and quantum electron scattering (QUEST) techniques, allowed one to understand why the Cooper minimum is located at 53.5 eV in the HHG spectra while it shows up at 50 eV in total photoionization cross-section (PICS) measurements [31,32]: on the one hand, HHG-based photorecombination is highly differential, contrary to total PICS, which induces a first blue shift of ∼1 eV; on the other hand, the decrease of the electron returning density with increasing electron energy further shifts the minimum to ∼53.5 eV.

Recently Shiner *et al.* [33] reported HHS measurements on Kr. The linearly polarized driving pulse has a 1.8-μm wavelength with a maximum intensity $I_0 = 1.8 \times 10^{14}$ W/cm^2, so that the HHG cutoff stands at ∼190 eV. Such an energy range is (largely) broad enough to include the Cooper minimum which is expected to appear, according to PICS measurements [31,32,34,35] and simulations [36], at ∼85 eV.

As a matter of fact, Shiner *et al.* did observe a minimum at about 85–90 eV in the HHG signal stemming from the so-called short [37] trajectories. The published experimental spectrum also presents an unexpected local maximum around 130 eV. We present here CTMC-QUEST simulations of the Schiner experiment which indicate that the peculiar shape of the HHG spectrum results from the shortness of the pulse. This pulse, corresponding to 1.8 optical cycles at half maximum, let half-cylce cutoffs [38,39] appear and shape the spectrum. The computed spectrum exhibits a minimum at 83 eV. The overall agreement with the measurements is satisfactory, except in the crucial ∼85-eV region where second-order diffraction seems to distort the experimental spectrum. However, the global agreement is good enough to state that HHG in Kr can be described in the SAE framework, as for Ar, provided the model potential describing the interaction of the active valence electron with the ionic core is adequately built.

Our paper is organized as follows: our CTMC-QUEST approach is outlined in Sec. II, putting special emphasis on the definition of the mean-field potential; the results of our simulations, including various carrier-envelope phases, intensities, and forms of laser pulses are presented in Sec. III; concluding remarks are finally given in Sec. IV. Atomic units are used unless otherwise stated.

II. CTMC-QUEST APPROACH TO HHG EMISSION

The CTMC-QUEST method has been described in details in [23] so that it will be only outlined herein. It merges a classical description of the first two steps of HHG, i.e., target ionization and electron propagation into the ionic continuum, and a quantum-mechanical representation of the recombination step. The approach employs the SAE approximation so that a mean-field (spherical) potential [29] has first to be designed to represent the interaction of the valence electron with the ionic core which is assumed to remain frozen throughout the interaction.

A. Design of a model potential for Kr valence electron dynamics

In [40], Le *et al.* noted that the location of the Cooper minimum in the HHG spectra of Ar significantly depends on the model potential employed within SAE simulations. Therefore particular care must be taken to the design of this potential. Here we employ a parametric potential of the form

$$V_{\rm mod}(r) = -\frac{Z-N}{r} - \frac{A\exp(-Br)+(N-A)\exp(-Cr)}{r}, \tag{1}$$

where $Z = 36$ is the nuclear Kr charge, $N = 35$ is the number of core electrons, and $\{A,B,C\}$ are positive parameters so that $V_{\rm mod}$ fulfills the expected limits $V_{\rm mod}(r) \to_{r\to\infty} -(Z-N)/r$ and $V_{\rm mod}(r) \to_{r\to 0} -Z/r$. The numerical values of the parameters are usually optimized to reproduce as accurately as possible the valence state energies of Kr. In practice, the optimization consists of diagonalizing iteratively the one-electron Hamiltonian $H = -\nabla^2/2 + V_{\rm mod}$ with varying A, B, and C until diagonalization yields eigenenergies that match reference data. In our case, the energies of reference are those tabulated in the NIST Atomic Spectral Database [41], and

TABLE I. Kr(nl) valence electron binding energies (in a.u.) obtained from model potential calculations with large-scale Slater basis (see text) compared to reference data taken from NIST [41] for Kr[$4s^2 4p^5\,(^2P_{3/2})\,nl$] levels (statistically averaged on j values). $V_{\rm mod}$(I) and $V_{\rm mod}$(II) distinguish two model potentials considered in the present work, as discussed in Sec. II A.

Level	NIST	$V_{\rm mod}$(I)	$V_{\rm mod}$(II)
$4p$	−0.514 48	−0.513 97	−0.514 46
$4d$	−0.066 70	−0.066 46	−0.070 56
$4f$	−0.031 46	−0.031 35	−0.031 37
$5s$	−0.148 48	−0.148 26	−0.147 08
$5p$	−0.093 07	−0.092 96	−0.092 11
$5d$	−0.036 54	−0.036 75	−0.038 23
$5f$	−0.020 13	−0.020 08	−0.020 09
$6s$	−0.060 09	−0.060 25	−0.059 77
$6p$	−0.044 30	−0.044 50	−0.044 16
$6d$	−0.022 87	−0.022 91	−0.023 58
$6f$	−0.013 96	−0.013 94	−0.013 95

H is diagonalized in a large-scale basis of even-tempered Slater-type orbitals (see [42] for details). Importantly, the underlying basis has to be really large enough to be considered as effectively complete (see [42,43] for details).

This first optimization procedure yields $A = 5.250$, $B = 0.902$, and $C = 3.640$. In Table I, we compare the energies of our computed Kr eigenstates with the reference data taken from NIST, focusing on the lowest bound states which are the most affected by the core. One can observe a very good agreement between both sets of data, the largest difference not exceeding 5.5×10^{-4} a.u. Beyond eigenenergies, it is quite common to further check the accuracy of the $V_{\rm mod}$ description at the level of eigenfunctions, by comparing oscillator strengths with reference data issued from either experiments or theoretical descriptions beyond the SAE approximation (see, e.g., [42]). We are not aware of such reference data for Kr. However, Huang *et al.* [36] have reported total and differential PICS obtained by means of the relativistic random phase approximation (RRPA) approach, which includes electronic correlations and associated multichannel interactions. Since the third step of HHG, i.e., photorecombination, is directly linked to differential photoionization through detailed balancing [29], those RRPA calculations are ideal probes of the accuracy of the $V_{\rm mod}$ description of HHG. Focusing on photoionization in the forward direction where the electron is ejected from the ϕ_{4p_z} initial state in the $\hat{\mathbf{z}}$ direction, the differential PICS is expressed as

$$\frac{d\sigma_{\rm PI}}{d\Omega_{\mathbf{k}}} = \frac{4\pi^2}{c} k\omega \left|\langle \Psi_{\mathbf{k}}^- | \hat{\mathbf{z}}\cdot\mathbf{r} | \phi_{4p_z}\rangle\right|^2, \tag{2}$$

where $\mathbf{k}$ is the ejected electron wave vector, ω is the photon frequency, and c the velocity of light. $\Psi_{\mathbf{k}}^-$ is the ingoing scattering continuum state, normalized on the $\mathbf{k}$ scale so that its partial-wave decomposition onto the spherical continuum states $\phi_{klm}(\mathbf{r}) = R_{kl}(r)Y_l^m(\theta_{\mathbf{r}},\varphi_{\mathbf{r}})$ is

$$\Psi_{\mathbf{k}}^-(\mathbf{r}) = \frac{1}{k}\sum_{l=0}^{\infty}\sum_{m=-l}^{l} i^l e^{-i\delta_{kl}} R_{kl}(r) Y_l^m(\Omega_{\mathbf{r}}) Y_l^{m^*}(\Omega_{\mathbf{k}}), \tag{3}$$

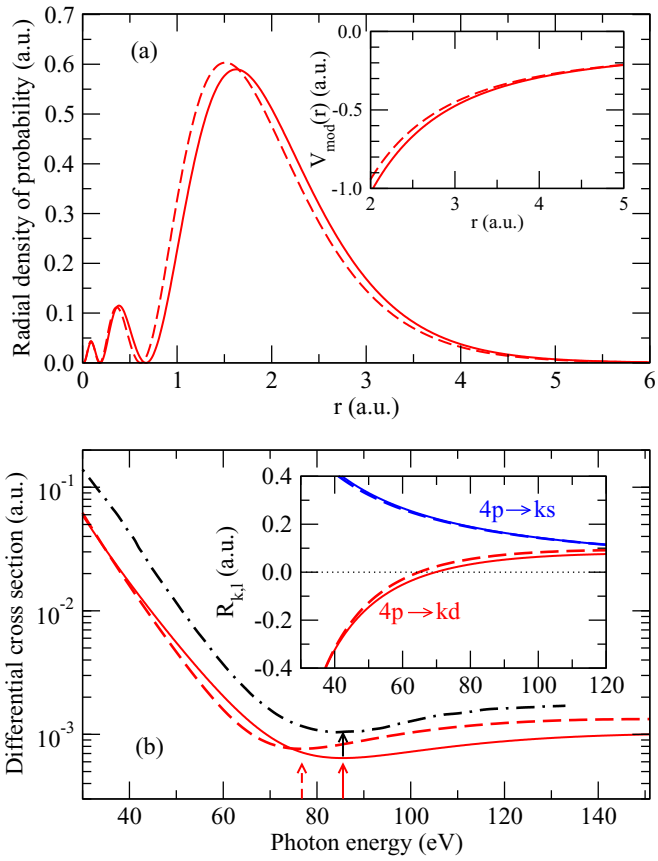

FIG. 1. (Color online) (a) Radial densities of probability for the fundamental Kr($4p$) state, obtained by means of the $V_{\rm mod}$(I) (- -) and $V_{\rm mod}$(II) (—) model potentials described in Sec. II A; $V_{\rm mod}$(I) (- -) and $V_{\rm mod}$(II) (—) are compared in the inset as functions of the radial coordinate r. (b) Differential photoionization cross section for Kr($4p$) in the forward direction as a function of the incident photon energy, obtained by means of the $V_{\rm mod}$(I) (- -) and $V_{\rm mod}$(II) (—) descriptions, compared to the RRPA cross section (– - –) of Huang *et al.* [36]; in the inset are displayed the radial integrals $\mathcal{R}_{k0}$ and $\mathcal{R}_{k2}$, associated with $V_{\rm mod}$(I) (- -) and $V_{\rm mod}$(II) (—), and involved in the definition of the cross section [see Eq. (4)].

where δ_{kl} are the phase shifts depending on both k and l. Inserting Eq. (3) into Eq. (2) and making use of $\phi_{4p_z} = R_{4p}(r)Y_1^0(\Omega_{\mathbf{r}})$, an explicit expression of the differential PICS (2) is obtained

$$\frac{d\sigma_{\rm PI}}{d\Omega_{\mathbf{k}}} = \frac{\pi}{3c}\frac{\omega}{k}|\mathcal{R}_{k0}e^{-i\delta_{k0}} - 2\mathcal{R}_{k2}e^{-i\delta_{k2}}|^2, \tag{4}$$

where $\mathcal{R}_{kl} = \int_0^\infty R_{kl}R_{4p}r^3dr$ are radial integrals linking the initial $4p$ and final continuum states. We display in Fig. 1(b) the comparison of our differential PICS with its RRPA counterpart. While both results present a similar shape, a significant shift is clearly visible between them: RRPA yields a Cooper minimum located around 85 eV while the $V_{\rm mod}$ approach moves it to 78 eV. On the one hand, the similarity of the shapes indicates that dynamical electron correlations do not drastically influence the photoionization process, contrary to what happens in Xe [20,21]. In other words, the electron-core interaction could be described in the framework of a mean-field (average) approach. On the other hand, the present $V_{\rm mod}$ potential does not represent accurately enough this mean field, and the Cooper minimum is misplaced.

Therefore we have decided to implement an optimization procedure of $V_{\rm mod}$ more adequate to HHG. Besides eigenenergies, we constrained the mean-field description to yield a shape of differential PICS similar to the RRPA one, using a least-squares fitting method. This approach has led to the $V_{\rm mod}$ parameters $A = 6.42$, $B = 0.905$, and $C = 4.20$. The resulting eigenenergies are given in Table I and named $V_{\rm mod}$(II) to differentiate them from our previous [$V_{\rm mod}$(I)] calculations. The agreement with NIST values is not as good as when we employ $V_{\rm mod}$(I), which has to be expected since the present least-squares fit includes additional constraints, but it remains very satisfactory. The energy of the fundamental $4p$ state is precisely reproduced, and the most noticeable difference concerns low-lying n states of d symmetry. Our new differential PICS is presented in Fig. 1(b). Its shape closely resembles that of the RRPA cross section, with a Cooper minimum appearing at 85 eV. $V_{\rm mod}$(II) thus describes the electron-core average interaction more satisfactorily than $V_{\rm mod}$(I), and therefore we will use it in our dynamical calculations. Before presenting these calculations, we illustrate the reasons for the shift of the Cooper minimum between the two $V_{\rm mod}$ calculations. In the inset of Fig. 1(a) we show that differences between $V_{\rm mod}$(I) and $V_{\rm mod}$(II) appear in the inner $r \lesssim 4$ a.u. region; they both behave as $-1/r$ for larger r [see Eq. (1)]. Around the energy of the fundamental Kr state ($\sim$−0.5 a.u.), $V_{\rm mod}$(II) has a slightly longer range than $V_{\rm mod}$(I); this induces a (small) shift of the Kr fundamental eigenstate issued from $V_{\rm mod}$(II) calculations towards larger r, as shown in Fig. 1(a) by means of the comparison of the radial densities of probability. This also influences the radial bound-free integrals (as well as the associated phase shifts) entering the definition (4) of the differential PICS, as shown in the inset of Fig. 1(b). All of this leads to the shift observed for the Cooper minimum.

B. CTMC-QUEST approach

1. *CTMC ionization and propagation until recombination*

The CTMC approach [44] employs an $\mathcal{N}$-point discrete representation of the phase-space distribution $\varrho(\mathbf{r},\mathbf{p},t)$ in terms of independent electron trajectories $\{\mathbf{r}_i(t),\mathbf{p}_i(t)\}$

$$\varrho(\mathbf{r},\mathbf{p},t) = \frac{1}{\mathcal{N}}\sum_{i=1}^{\mathcal{N}}\delta(\mathbf{r}-\mathbf{r}_i(t))\delta(\mathbf{p}-\mathbf{p}_i(t)). \tag{5}$$

Here $\mathcal{N} = 40 \times 10^6$ in order to fulfill statistical convergence.

At $t = 0$, the initial distribution is usually defined as a microcanonical set where all trajectories have the energy of the initial quantum state, i.e., $E_i(t=0) = p_i^2(t=0)/2 + V_{\rm mod}(r_i(t=0)) = -I_P$ where I_P is the ionization potential. However, such a distribution does not properly span the (classical forbidden) $r > 1/I_P$ region of the phase space. As a consequence, the transitions to excited and ionizing states, which involve outer electron trajectories, are underestimated [45–48]. It was thus proposed in the latter references (and works cited therein) to use an improved distribution which better matches the quantum distribution in both configuration and momentum spaces. In this work, we use a Wigner-like

distribution [47,48] built as a sum of 40 microcanonical sets with an average energy $-I_P$. The energy spread of the improved distribution is given by the partition of the classical phase space into adjacent and nonoverlapping energy bins that mimics the quantization of bound states (see [23,48,49] for details). Here the electron trajectories have initial energies lying between -0.8 and -0.15 a.u. This energy spread is at the root of the improved description of ionization (see [50–52] as well as the previous references [45–48]).

Once the initial distribution is defined, its subsequent evolution is described by the motion of the $\mathcal{N}$ independent trajectories tailored by Hamilton's equations

$$\frac{\partial \mathbf{r}_j(t)}{\partial t} = \mathbf{p}_j(t), \tag{6}$$

$$\frac{\partial \mathbf{p}_j(t)}{\partial t} = -\boldsymbol{\nabla}_{\mathbf{r}}[V_{\text{mod}}(r) + \mathbf{r}\cdot\mathbf{F}(t)]|_{\mathbf{r}_j(t)}, \tag{7}$$

where $\mathbf{r}\cdot\mathbf{F}(t)$ is the laser-Kr interaction expressed in the length gauge, within the dipolar approximation. It is clear from Eq. (7) that CTMC treats the ionic (V_{mod}) and laser [$\mathbf{F}(t)$] fields on the same footing, beyond the well-known strong-field approximation (SFA, [37]) that neglects the ionic field and therefore leads to unfair descriptions of harmonic features close to the ionization threshold [53].

The CTMC calculations are gauge independent: in the length gauge, combining Eqs. (6) and (7) yields Newton's law $\ddot{\mathbf{r}}_j(t) = -\boldsymbol{\nabla}_{\mathbf{r}} V_{\text{mod}}(r)|_{\mathbf{r}_j(t)} - \mathbf{F}(t)$; in the velocity gauge, the total Hamiltonian is expressed as $H = \mathbf{p}^2/2 + V_{\text{mod}}(r) + \mathbf{p}.\mathbf{A}(t)$, where $\mathbf{A}(t)$ is the laser potential vector, so that Hamilton's equations are $[\partial \mathbf{r}_j(t)/\partial t = -\boldsymbol{\nabla}_{\mathbf{r}} V_{\text{mod}}(r)|_{\mathbf{r}_j(t)}, \partial \mathbf{p}_j(t)/\partial t = \mathbf{p}_j(t) + \mathbf{A}(t)]$, leading to the same Newton's law $\ddot{\mathbf{r}}_j(t) = -\boldsymbol{\nabla}_{\mathbf{r}} V_{\text{mod}}(r)|_{\mathbf{r}_j(t)} - \mathbf{F}(t)$, since $\mathbf{F}(t) = -\dot{\mathbf{A}}(t)$.

In the present work, the electric laser pulse $\mathbf{F}(t)$ is defined so as to mimic the pulse employed in the experiment of Shiner *et al.* [33]; in practice we employ a linearly polarized $\sin^2$-shaped pulse

$$\mathbf{F}(t) = F_0 \sin^2\left(\frac{\pi t}{\tau}\right)\cos\left(\omega_0 t - \frac{\omega_0 \tau}{2} + \phi_{\text{CE}}\right)\hat{\mathbf{z}} \tag{8}$$

of pulsation $\omega_0 = 0.025\,33$ a.u., maximum amplitude F_0 such that $I_0 = \epsilon_0 c F_0^2/2$, and total duration $\tau = 909.1$ a.u. (corresponding to 1.8 optical cycles at half maximum). While the HE-TOPAS parametric amplifier employed in [33] guarantees a fixed carrier-envelope phase ϕ_{CE} from shot to shot [54], its absolute value has not been measured; we will accordingly make (separate) simulations with ϕ_{CE} varying from 0, where $F(t = \tau/2) = F_0$, to $3\pi/4$. Alternatively to Eq. (8), we have also considered a Gaussian-shaped pulse defined to comprise 1.8 optical cycles at half maximum, like Eq. (8); simulations employing such a pulse led to results almost identical to those using Eq. (8), at least in the $\gtrsim 40$ eV energy region of interest. Therefore all the results presented in the next section correspond to computations using the $\sin^2$-shaped pulse (8).

Driven by the laser field, some trajectories come back to the ionic core onto which they may recombine to give rise to HHG. However, describing quantitatively recombination within purely classical statistics is unrealistic because the recombination probability is so low that we would have to discretize the phase-space distribution in terms of billions of trajectories. We circumvent this problem by assuming that every electron which returns to the vicinity of the ionic core forms a part of a recolliding wave packet amenable to HHG through (quantum) recombination. In practice, we define a recombination sphere, centered on the target nucleus, of radius R_{rec} of the order of the extension of the fundamental Kr wave function. Then, simply counting the number of electrons which have been ionized, left the sphere, and entered back into it at time t_i allows us to obtain the returning electron density, integrated over the whole laser-target interaction time, as

$$\varrho_{\text{ret}}(E,\hat{\mathbf{k}}) = \frac{1}{\mathcal{N}}\sum_i \delta(E_i(t_i) - E)\delta(\hat{\mathbf{k}}_i(t_i) - \hat{\mathbf{k}}), \tag{9}$$

where $E_i(t_i)$ and $\mathbf{k}_i(t_i)$ are the energy and the direction of the wave vector of the returning electron when this latter enters the recombination sphere of radius R_{rec}. Photorecombination of the trajectory is assumed to occur suddenly at time t_i. Here we set $R_{\text{rec}} = 5$ a.u. but we explicitly checked, as in [23], that varying R_{rec} around this selected value does not change the shape of ϱ_{ret}. For a given couple $(E,\hat{\mathbf{k}})$, CTMC allows us to discriminate between short, long, and even multiple return trajectories by means of a simple $[t_i, E_i(t_i)]$ mapping [48]; this is one of the advantages of the CTMC-QUEST approach.

2. *QUEST recombination*

Once a returning electron enters the recombination sphere at time t_i with energy E_i in the direction $\hat{\mathbf{k}}_i$, sudden photorecombination leads to emission of a HHG photon of frequency $\omega = E_i + I_P$ with probability $\mathcal{P}_{\text{PR}}(E_i,\hat{\mathbf{k}}_i)$. Counting among the $\mathcal{N}$ independent trajectories those which fulfill this criterion allows us to define the time-integrated HHG yield with frequency ω as

$$S(\omega) = \int dE\, \varrho_{\text{ret}}(E,\hat{\mathbf{k}})\mathcal{P}_{\text{PR}}(E,\hat{\mathbf{k}})\delta(E + I_P - \omega), \tag{10}$$

where $\mathcal{P}_{\text{PR}}(E,\hat{\mathbf{k}})$ is the probability rate for (field-free) photorecombination of an electron impinging on the ionic core in the $\hat{\mathbf{k}}$ direction with energy E. Since the driving laser is linearly polarized along the z axis, the harmonic radiation is also polarized in the $\hat{\mathbf{z}}$ direction.

Assuming that the wave-packet component associated with each returning electron has unit amplitude, the total flux j_{ret} of returning electrons is linked to the total density ϱ by $j_{\text{ret}}(E,\hat{\mathbf{k}}) = \varrho_{\text{ret}}(E,\hat{\mathbf{k}})\mathbf{k}$; under the same assumption, photorecombination rate and cross section are related to each other through $\mathcal{P}_{\text{PR}}(E,\hat{\mathbf{k}}) = \sigma_{\text{PR}}(E,\hat{\mathbf{k}})\mathbf{k}$. It follows from these relations that the HHG yield (10) can be expressed as $S(\omega) = j_{\text{ret}}(E,\hat{\mathbf{k}})\sigma_{\text{PR}}(E,\hat{\mathbf{k}})$, with $\omega = E + I_P$, which is the factorization formula resulting from time-dependent effective range theory [55] and employed within quantitative rescattering schemes [40,56]. For a given value of energy E, the mean value of $\hat{\mathbf{k}}$, computed as the average of $\hat{\mathbf{k}}_i$ among the $\mathcal{N}_{\text{ret}}$ trajectories that come back into the recombination sphere with $E_i = E$, is $\mathbf{0}$. The factorization then simplifies to $S(\omega) = j_{\text{ret}}(E,0^\circ)\sigma_{\text{PR}}(E,0^\circ)$. Note that in the case of elliptically polarized driving fields and nonisotropic target initial states, such a single factorization is not possible since primary tunnel ionization selects a quantization axis slanted

with respect to the main axis of the driving field. $S(\omega)$ then involves orthogonal components at 0° and 90° [57]. However, the statistical CTMC-QUEST approach can still be applied in such cases [8].

Because of the discretized (statistical) nature of $\varrho_{\rm ret}$ [Eq. (9)], Eq. (10) transforms into

$$S(\omega) = \frac{1}{\mathcal{N}} \sum_{i=1}^{\mathcal{N}_{\rm ret}} \mathcal{P}_{\rm PR}(E_i, \hat{\mathbf{k}}_i) W(E_i, \Delta E), \tag{11}$$

where $W(E_i, \Delta E)$ is a rectangular window function such that $W(E_i, \Delta E) = 0$ if $|\omega - E_i - I_P| > \Delta E/2$ and $W(E_i, \Delta E) = 1$ otherwise. In the following illustrations, $\Delta E = 1$ eV, but we explicitly checked that the shape of $S(\omega)$ is not changed when $\Delta E = 0.5$ or 2 eV.

The photorecombination rate $\mathcal{P}_{\rm PR}$ is computed by means of the Fermi golden rule [29], which gives

$$\mathcal{P}_{\rm PR}(E, \hat{\mathbf{k}}) = \frac{1}{2\pi} \frac{\omega^3}{c^3} \left| \langle \phi_{4p_z} | \hat{\mathbf{z}}.\mathbf{r} | \Psi_{\mathbf{k}}^+ \rangle \right|^2, \tag{12}$$

with $\omega = E + I_P$ as before. Equation (12) is consistent with the expression (2) of the differential PICS, since $\sigma_{\rm PR} = 8\pi^3 \mathcal{P}_{\rm PR}/k$ as $\Psi_{\mathbf{k}}^+$ is normalized on the wave-vector scale, and $\sigma_{\rm PI} = k^2 c^2 \sigma_{\rm PR}/\omega^2$ because of the principle of detailed balancing [29]. Finally it is worth recalling that replacing the stationary scattering state $\Psi_{\mathbf{k}}^+$ in Eq.(12) by its plane-wave approximation distorts not only the representation of HHG features close to the ionization threshold but also the description of Cooper minima [10,23]; the ionic potential is of paramount importance in the three steps of the HHG process.

III. RESULTS

A. A pulse with $I_0 = 1.8 \times 10^{14}$ W/cm^2 and $\phi_{\rm CE} = 0$

We first present the CTMC-QUEST results corresponding to the driving laser field of Eq. (8) with maximum intensity $I_0 = 1.8 \times 10^{14}$ W/cm^2 and carrier-envelope phase $\phi_{\rm CE} = 0$. This field, displayed in Fig. 2(a), presents four half-cycle maxima of large enough amplitude to ionize the Kr target and subsequently lead to HHG. We superimpose onto the field the energy E of the rescattering electron trajectories as a function of their photorecombination time, and four arches indeed appear in the course of the interaction. As is well known [37,53], each arch is composed of short (left) and long (right) branches which coalesce at the HHG cutoff corresponding to the maximum energy that can be gained by the electron through propagation in the continuum.

Among all these rescattering trajectories, we mimic the experimental detection [33] by isolating the short ones, and we plot in Fig. 2(b) the associated returning density $\rho_{\rm ret}(E)$ integrated over the $\hat{\mathbf{k}}$ directions, $\rho_{\rm ret}(E) = \int \varrho_{\rm ret}(E, \hat{\mathbf{k}}) d\hat{\mathbf{k}}$, as a function of the emitted photon energy $\omega = E + I_P$. Three half-cycle cutoffs clearly show up in $\varrho_{\rm ret}$, corresponding to the tops of the three first arches of Fig. 2(a); a weak density is associated with the fourth arch, located at ($t \sim 750$ a.u., $E \sim 30$ eV) in Fig. 2(a), so that it is hidden in the background of the more energetic contributions in Fig. 2(b). Beyond the conspicuous cutoffs, the electron density associated with one short branch of an arch presents a slightly decreasing shape as E increases, until the cutoff is reached where $\varrho_{\rm ret}$ peaks. Such

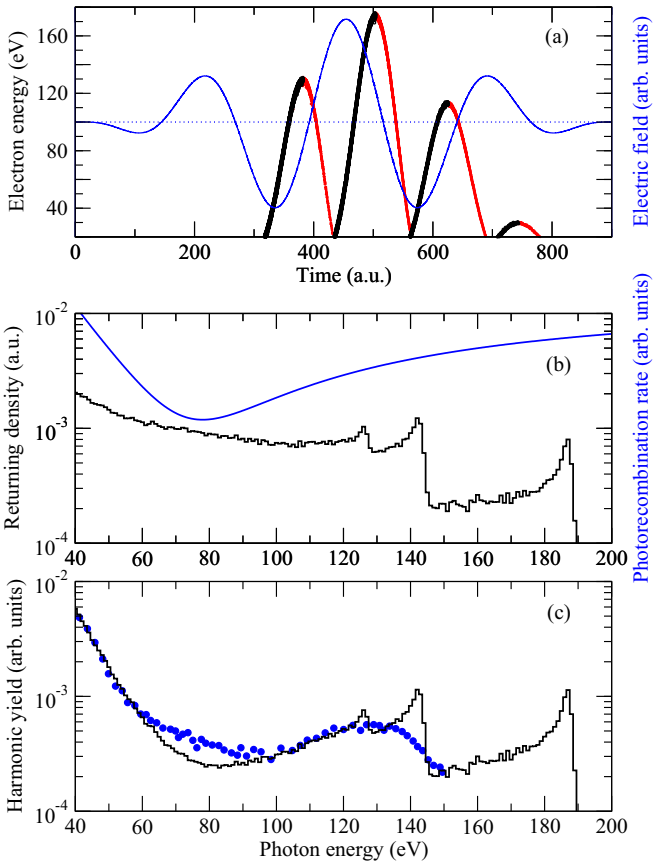

FIG. 2. (Color online) (a) Temporal evolution of the field [Eq. (8)] with $\lambda = 1800$ nm, $I_0 = 1.8 \times 10^{14}$ W/cm^2, and $\phi_{\rm CE} = 0$ (blue thin line) to which are superimposed the energies $E_i(t)$ of the short [dark (black) points] and long [light (red) points] trajectories at time of recombination. (b) Time- and angle-integrated returning electron density of short trajectories (black histogram) and photorecombination rate at zero degree (blue line), as functions of the emitted photon energy $\omega = E_i + I_P$. (c) Computed (black histogram) and experimental [33] (blue circles) HHG spectra.

behavior is noticeable in the 40–125 eV photon energy range in Fig. 2(b), corresponding to the short branch of the third arch in Fig. 2(a). Two opposite effects are at play to determine the behavior of $\varrho_{\rm ret}(E)$ with E. First, longer trajectories are born at earlier times when the laser field is more intense and thus benefit from stronger ionization rates; this implies an increase of $\varrho_{\rm ret}(E)$ as E increases. However, longer trajectories are also subject to a stronger lateral displacement during propagation in the continuum, which induces $\varrho_{\rm ret}(E)$ to decrease as E increases. Combining these two effects then leads to the typical shape of $\varrho_{\rm ret}(E)$ appearing in Fig. 2(b) between 40 and 125 eV. Note that multiplying $\varrho_{\rm ret}(E)$ by $k = \sqrt{2E}$ to obtain the flux of returning electrons, commonly referred to as the returning wave packet in quantitative rescattering theories [40,56], one obtains an essentially flat profile as a function of E, consistent with the findings of [40].

Since the harmonic yield $S(\omega)$ basically consists of the product of the returning density $\varrho_{\rm ret}$ and photorecombination rate $\mathcal{P}_{\rm PR}$ [see Eq. (10)], we include in Fig. 2(b) $\mathcal{P}_{\rm PR}(E, 0°)$ as a function of $\omega = E + I_P$. The rate presents a minimum

at $\omega = 79$ eV, shifted with respect to the minimum of the differential PICS $\sigma_{\rm PI}(\omega,0^\circ)$ which is located at 85 eV [see Fig. 1(b)]; this shift is due to the different prefactors in $\mathcal{P}_{\rm PR}(E,0^\circ)$ and $\sigma_{\rm PI}(\omega,0^\circ)$, consistent with the principle of detailed balancing [see Eqs. (12) and (2)]. However, the descending shape of the returning density $\varrho_{\rm ret}$ in this energy range makes the Cooper minimum appear in the computed HHG yield around 83 eV, as displayed in Fig. 2(c). The location of the Cooper minimum in the HHG spectrum with respect to that observed in differential PICS measurements thus depends on the competition between the shift associated with transition from photoionization to photorecombination and the shift associated with the local shape of the returning wave packet. While the first shift dominates in Kr under the present irradiation conditions, leading to a Cooper minimum appearing at lower energy in the HHG spectrum (∼83 eV) than in the differential PICS (∼85 eV), the reverse applied in Ar [23] where the Cooper minimum in the HHG spectra was shifted by 3 eV towards high energies with respect to its location in differential PICS.

We compare in Fig. 2(c) the HHG yield $S(\omega)$ obtained by means of the present $V_{\rm mod}$ description with the experimental result of Shiner *et al.* [33], the latter being arbitrarily scaled to match the computed $S(\omega)$ at low energies. We judge that the agreement between the two results, far from being perfect, is satisfactory. The computed spectrum nicely matches its experimental counterpart for $\omega \leqslant 60$ eV and in the 100–130 eV energy region. For $\omega > 130$ eV, the experimental spectrum falls down while the calculations exhibit half-cycle cutoffs, as expected because of the shortness of the pulse [see Fig. 2(a)] and previously observed in Ref. [38]. Later on, we will investigate whether carrier-envelope phases $\phi_{\rm CE}$ different from 0 or averaging over the focal volume of the laser beam can improve the agreement between theory and experiment. Before this, it is important to note that in the crucial ∼85 eV energy range where CTMC-QUEST leads to a clear Cooper minimum, the measurements yield a seemingly filled hole. Such a filling can be due to second-order diffraction of the grating used to disperse the HHG spectrum; according to this mechanism, the local maximum observed at 130 eV indeed appears in second order at 65 eV, and this second-order peak, of lower magnitude, is amenable to fill in the Cooper minimum. Contamination of HHG spectra by second-order diffraction is usually avoided at low energies using Al filters [23,33]; this procedure cannot be used for a Kr target since the Al filters impede emission above 75 eV [33] which is the region of present interest.

If we admit second-order contamination, the agreement between the measured and computed HHG spectra of Kr is then quite satisfactory. This means that HHG dynamics in Kr can be accurately described within the SAE approximation that underlies the present CTMC-QUEST approach, provided the mean electron-core ionic field is suitably defined. As a matter of fact, a worse agreement is herein obtained with experiment if we use the $V_{\rm mod}$(I) potential instead of the optimized $V_{\rm mod}$(II) one.

B. Varying the carrier-envelope phase

The calculated HHG spectrum of Fig. 2(c) presents large half-cycle cutoffs which do not show up in the measurements.

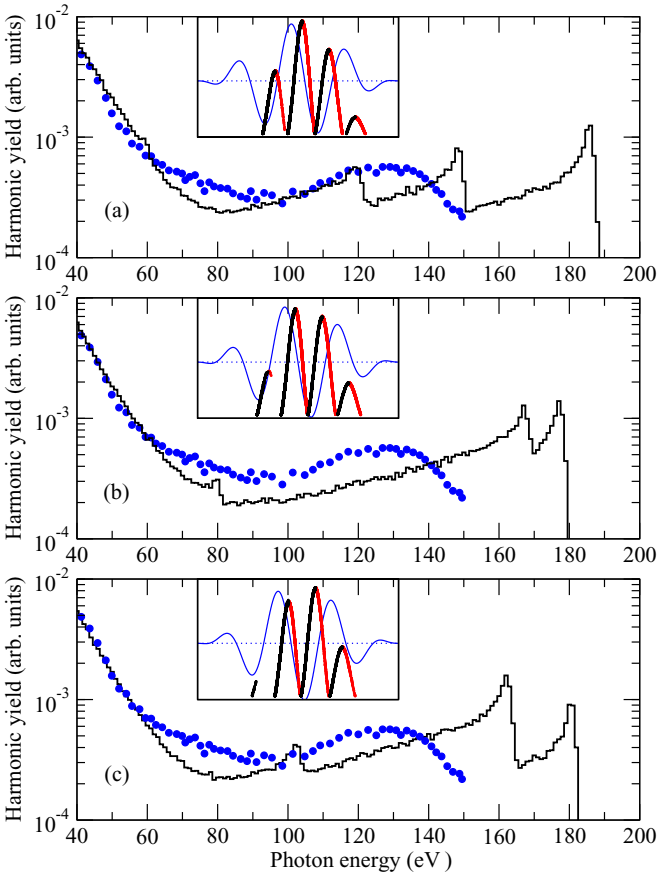

FIG. 3. (Color online) Computed (black histograms) and experimental [33] (blue points) HHG spectra for a driving field [Eq. (8)] with $\lambda = 1800$ nm, $I_0 = 1.8 \times 10^{14}$ W/cm^2, and $\phi_{\rm CE} = \pi/4$ (a), $\pi/2$ (b), and $3\pi/4$ (c). In the insets are displayed the temporal evolutions of the fields (thin blue lines) to which are superimposed the energies $E_i(t)$ of the short [dark (black) points] and long [light (red) points] trajectories at time of recombination, similar to Fig. 2(a).

As previously mentioned, the HE-TOPAS parametric amplifier employed in the experiment [33] guarantees a fixed carrier-envelope phase $\phi_{\rm CE}$ from shot to shot, but its absolute value has not been measured. $\phi_{\rm CE}$ controls the magnitude of the half-cycle maxima of the pulse electric field, and subsequently the energy of HHG half-cycle cutoffs. We therefore performed additional CTMC-QUEST calculations with $\phi_{\rm CE} = \pi/4, \pi/2$, and $3\pi/4$, with the aim of checking whether the agreement between theory and experiment is improved for $\phi_{\rm CE} \neq 0$, especially in the (cutoff) energy range 120–150 eV [see Fig. 2(c)].

Our results are given in Fig. 3. For each value of $\phi_{\rm CE}$, we display the pulse field $F(t)$ and the associated arches of returning trajectories as functions of time, similar to Fig. 2(a). The computed HHG yields stemming from short trajectories are then compared with the measurements of Shiner *et al.* Considering Fig. 2(c) and Figs. 3(a)–3(c), it is clear that the better agreement between CTMC-QUEST computations and experiment is obtained for $\phi_{\rm CE} = 0$, which we therefore venture to identify as the carrier-envelope phase of the pulse employed in [33].

C. Averaging over the focal volume

From now on, we thus consider that $\phi_{CE} = 0$. But we aim at taking into account that HHG occurs within the focal volume of the driving laser beam. As our model does not include phase-matching effects related to the propagation of harmonic light within the generating medium, considering the focal volume amounts to summing incoherently the harmonic yields associated with laser pulses with intensities decreasing from I_0, consistent with the waist of the beam. We assume a Gaussian spatial profile for the intensity of the the laser pulse; further, owing to the experimental details about the generation of the short 1800-nm pulse given in [33], associated with the fact that the last focusing mirror has a 25 cm focal length [58], we estimate that the radius of the (cylindrical) spot in the interaction region, located ∼2 mm after the focal point, is ∼55 μm.

In practice, additional CTMC-QUEST calculations have been performed for $I_0 = 1.71 \times 10^{14}$ and 1.62×10^{14} W/cm^2 which correspond to 95% and 90% of the former maximum intensity $I_0 = 1.8 \times 10^{14}$ W/cm^2, respectively. Constraining the transverse intensity dependence of the beam to these three intensities within a numerical scheme where the Gaussian profile is described by adjacent and nonoverlapping bins amounts to restricting the radius of the interaction region to 14.2 μm. The averaged HHG signal then consists of the (normalized) sum of the yields associated with the three intensities.

Our averaged HHG yield is presented in Fig. 4, together with the measurements of Shiner *et al.* The averaging smooths the conspicuous half-cycle cutoffs which appeared in Fig. 2(c) around 125–145 eV where we considered only a driving intensity $I_0 = 1.8 \times 10^{14}$ W/cm^2. This had to be expected since lowering the intensity I_0 leads to a shift of these cutoffs towards lower energies, so that the sum involved in the averaging yields a smoother shape of the total HHG yield. Beyond the second-order diffraction issue, the agreement of the averaged yield with measurements is now very satisfactory. However, additional measurements at higher energies would be useful to test the CTMC-QUEST calculations (and restricted averaging) in the whole energy range 40–190 eV.

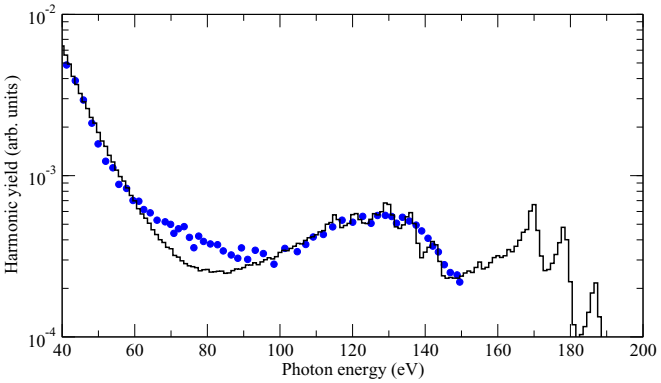

FIG. 4. (Color online) Computed HHG spectrum after averaging over the focal volume (black histogram), as defined in Sec. III C, compared to the experimental data [33] (blue points).

D. Driving sinusoidal fields

As atomic or molecular targets interact with (common) driving laser pulses of 30 fs duration or so, HHG spectra do not generally exhibit half-cycle cutoffs, because of the superposition of underlying adjacent contributions associated with the cycles comprising the shaped pulse (similar with what happened in the previous averaging), or because of moderate intensities such that HHG mainly occurs around the maximum field strength. To mimic such an interaction with reduced computational cost, one can use a simple sinusoidal driving field $F(t) = F_0 \sin(\omega_0 t)$ associated with an effective intensity $I_0 = \epsilon_0 c F_0^2/2$. Furthermore $t \in [0, 1.25/\omega]$ so that multiple-return trajectories do not contribute to HHG while above-threshold short and long trajectories are all included [37,48].

Here we still consider $\omega_0 = 0.025\,33$ a.u. (corresponding to wavelength $\lambda = 1800$ nm) and two distinct values of I_0, $I_0 = 1.2 \times 10^{14}$ and $I_0 = 1.8 \times 10^{14}$ W/cm^2, respectively. Our results are displayed in Fig. 5 which includes two columns, the left one being related to $I_0 = 1.2 \times 10^{14}$ W/cm^2 while the right one is associated with $I_0 = 1.8 \times 10^{14}$ W/cm^2. In the first row of this figure, we show the sinusoidal laser fields together with the $[t, E(t)]$ mapping which illustrates the energy $E(t)$ of

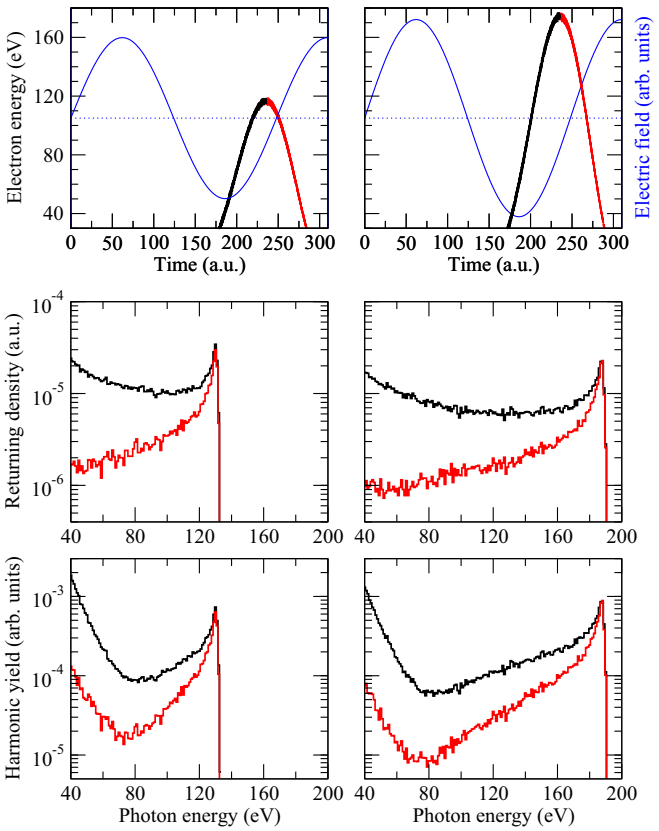

FIG. 5. (Color online) Calculations for driving sinusoidal fields (Sec. III D) with $I_0 = 1.2 \times 10^{14}$ W/cm^2 (left column) and $I_0 = 1.8 \times 10^{14}$ W/cm^2 (right column) for short (dark black) and long (light red) trajectories. Top row: Temporal evolution of the fields (blue thin line) to which are superimposed the energies $E_i(t)$ of the short and long trajectories at the time of recombination. Middle row: Time- and angle-integrated returning electron density of short and long trajectories. Bottom row: Computed HHG spectra for short and long trajectories.

the rescattering electrons as a function of the recombination time t. The short and long branches form one arch that ends up at the maximum energy $E_{\max} = 0.3I_P + 3.17U_P$, so that the maximum energy of the harmonic photons will fulfill the well-known scaling $\omega_{\max} = 1.3I_P + 3.17U_P$ [37]; in the previous cases of shaped fields, this scaling does not apply exactly.

We separate the short and long contributions to the arch, and we display in the second row of Fig. 5 the associated (angle-integrated) electron densities $\rho_{\rm ret}^{\rm (short,long)}(E)$ as functions of $\omega = E + I_P$. We have already commented in the present paper on the mechanisms responsible for the shape of $\rho_{\rm ret}^{\rm (short)}(E)$. Contrary to this latter, $\rho_{\rm ret}^{\rm (long)}(E)$ monotonically increases as E increases. Among the long trajectories, those with lower E were born around the first maximum field strength, at $t \sim T = 2\pi/\omega_0$, and thus benefit from strong ionization rates. However, they recombine later, up to $t \sim 1.25T$, and are then subject to strong lateral displacements which minimize the recombination probability. The reverse applies for long trajectories with high E: born later than the trajectories with low E, they experience lower ionization rates; but they benefit from higher recombination probabilities because of smaller times of flight. Therefore the increasing shape of $\rho_{\rm ret}^{\rm (long)}(E)$ indicates that for long trajectories, electron propagation into the continuum (and correlated effect on recombination) plays the major role. $\rho_{\rm ret}^{\rm (short)}(E)$ and $\rho_{\rm ret}^{\rm (long)}(E)$ coincide at the cutoff energy $E_{\max}$, where short and long trajectories cannot be distinguished from each other.

We present in the last row of Fig. 5 the computed HHG yields associated with short and long trajectories, $S^{\rm (short)}(\omega)$ and $S^{\rm (long)}(\omega)$, respectively. The Cooper minimum appears in both $S^{\rm (short)}$ and $S^{\rm (long)}$ but its location on the photon energy scale depends on the type of trajectories; for instance, at $I_0 = 1.2 \times 10^{14}$ W/cm^2, the minimum is located at $\omega = 83$ eV in $S^{\rm (short)}(\omega)$ and at $\omega = 75$ eV in $S^{\rm (long)}(\omega)$. We explained in Sec. III A how the decreasing shape of $\rho_{\rm ret}^{\rm (short)}(E)$ around $E \sim 80$ eV induces a blue shift of the minimum in $S^{\rm (short)}(\omega)$. This still happens here. For long trajectories, $\rho_{\rm ret}^{\rm (long)}(E)$ is increasing as E increases so that the shift of the Cooper minimum with respect to that appearing in the differential photorecombination cross section occurs in the reverse direction, towards low photon energies. Finally, the dependence of the minimum position on the intensity of the driving field is rather weak: varying I_0 from 1.2×10^{14} to 1.8×10^{14} W/cm^2 results in a shift of the minimum of $\sim$2 eV towards high energies. This behavior stems from the local variations of the shapes of $\rho_{\rm ret}^{\rm (short,long)}(E)$ with I_0. As I_0 is (largely) increased, the HHG cutoff is pushed back to high $\omega_{\max}$ so that the decreasing shape of $\rho_{\rm ret}^{\rm (short)}(E)$ around 80 eV is accentuated while the increasing shape of $\rho_{\rm ret}^{\rm (long)}(E)$ is softened.

IV. CONCLUSIONS

We have performed semiclassical calculations of high-order-harmonic generation in Kr in order to simulate recent experiments on high-order-harmonic spectroscopy of the Cooper minimum by Shiner *et al.* [33]. The agreement between theory and experiment is rather satisfactory even if the Cooper minimum, which clearly shows up in the computations around 83 eV, is blurred in the experimental spectrum probably because of second-order diffraction of the grating used to disperse the harmonics.

The calculations employed the single-active electron approximation, in which the inner shells of Kr are assumed to remain frozen throughout the HHG dynamics. The agreement with experiment therefore indicates that the HHG dynamics in Kr can be described reliably in the single-active electron framework, as for Ar. However, we carefully refrain from stating that this is generally the case, even for rare-gas atoms. Xe, in which dynamical multichannel interactions shape both photoionization cross sections and harmonic spectra [20,21], is the counterexample. Nevertheless we state that for Cooper minima in atoms, whose features have been described in terms of properties related to valence electrons since the pioneering work of Cooper [28], Xe is a quite special case so that the single-active electron approximation can safely be applied for most systems, provided sufficient care has been taken to represent the mean field between the valence electron and the ionic core. We do not extend this to molecules where inner shells, lying close to the valence one on the energy scale, can actively participate in the dynamics [16].

Concerning Kr, additional measurements would be desirable to test further the present semiclassical calculations over an extended energy range. Longer pulse durations would prevent the appearance of half-cycle cutoffs, especially in the 120–140 eV region which contaminates the Cooper minimum through second-order diffraction. Dividing the observed spectrum by the RRPA photorecombination cross section would thus yield an experimental estimate of the returning electron wave packet that could be compared to our single-active electron calculations, to definitely elicit whether electron correlations play an important role in the first two steps of high-order-harmonic generation in Kr.

ACKNOWLEDGMENTS

The authors acknowledge B. Schmidt, F. Légaré, and D. Villeneuve for providing them with details about the experimental setup [33]. Financial support by the Conseil Régional d'Aquitaine is gratefully acknowledged as well as computational facilities provided by the Mésocentre de Calcul Intensif Aquitain at University of Bordeaux [59].

[1] J. B. West, J. Phys. B **34**, R45 (2001).
[2] K. L. Reid, Annu. Rev. Phys. Chem. **54**, 397 (2003).
[3] P. B. Klein and S. C. Binari, J. Phys. Condens. Matter **15**, R1641 (2003).
[4] P. Löffler *et al.*, Chem. Phys. Lett. **252**, 304 (1996).
[5] Y. Zhang, K. Yuan, S. Yu, D. H. Parker, and X. Yang, J. Chem. Phys. **133**, 014307 (2010).
[6] P. B. Corkum, Phys. Rev. Lett. **71**, 1994 (1993).
[7] K. Midorikawa, Jpn. J. Appl. Phys. **50**, 090001 (2011).
[8] D. Shafir *et al.*, Phys. Rev. Lett. **108**, 203001 (2012).

[9] D. Shafir, Y. Mairesse, D. M. Villeneuve, P. B. Corkum, and N. Dudovich, Nat. Phys. **5**, 412 (2009).
[10] H. J. Wörner, H. Niikura, J. B. Bertrand, P. B. Corkum, and D. M. Villeneuve, Phys. Rev. Lett. **102**, 103901 (2009).
[11] H. Lörch, N. Scherer, T. Kerkau, and V. Schmidt, J. Phys. B **32**, L371 (1999).
[12] M. Lebech, J. C. Houver, and D. Dowek, Rev. Sci. Instrum. **73**, 1866 (2002).
[13] J. Itatani *et al.*, Nature (London) **432**, 867 (2004).
[14] H. Ruf *et al.*, J. Chem. Phys. **137**, 224303 (2012).
[15] F. Lépine, M. Y. Ivanov, and M. J. J. Vrakking, Nat. Photon. **8**, 195 (2014).
[16] O. Smirnova *et al.*, Nature (London) **460**, 972 (2009).
[17] Y. Mairesse *et al.*, Phys. Rev. Lett. **104**, 213601 (2010).
[18] W. Li *et al.*, Science **322**, 1207 (2008).
[19] A.-T. Le, T. Morishita, R. R. Lucchese, and C. D. Lin, Phys. Rev. Lett. **109**, 203004 (2012).
[20] A. D. Shiner *et al.*, Nat. Phys. **7**, 464 (2011).
[21] S. Pabst and R. Santra, Phys. Rev. Lett. **111**, 233005 (2013).
[22] C. Vozzi, F. Calegari, F. Frassetto, L. Poletto, G. Sansone, P. Villoresi, M. Nisoli, S. De Silvestri, and S. Stagira, Phys. Rev. A **79**, 033842 (2009).
[23] J. Higuet *et al.*, Phys. Rev. A **83**, 053401 (2011).
[24] J. P. Farrell, L. S. Spector, B. K. McFarland, P. H. Bucksbaum, M. Gühr, M. B. Gaarde, and K. J. Schafer, Phys. Rev. A **83**, 023420 (2011).
[25] C. Jin and C. D. Lin, Phys. Rev. A **85**, 033423 (2012).
[26] S. Pabst, L. Greenman, D. A. Mazziotti, and R. Santra, Phys. Rev. A **85**, 023411 (2012).
[27] D. A. Telnov, K. E. Sosnova, E. Rozenbaum, and Shih-I Chu, Phys. Rev. A **87**, 053406 (2013).
[28] J. W. Cooper, Phys. Rev. **128**, 681 (1962).
[29] B. H. Bransden and C. J. Joachain, *Physics of Atoms and Molecules* (Prentice-Hall, Englewood Cliffs, NJ, 2003).
[30] H. G. Muller, Phys. Rev. A **60**, 1341 (1999).
[31] G. V. Marr and J. V. West, At. Data Nucl. Data Tables **18**, 497 (1976).
[32] J. Samson and W. Stolte, J. Electron Spectrosc. Relat. Phenom. **123**, 265 (2002).
[33] A. D. Shiner *et al.*, J. Phys. B **45**, 074010 (2012).
[34] S. Aksela, H. Aksela, M. Levasalmi, K. H. Tan, and G. M. Bancroft, Phys. Rev. A **36**, 3449 (1987).
[35] M. Richter *et al.*, AIP Conf. Proc. **652**, 165 (2003).
[36] K.-N. Huang and W. R. Johnson, At. Data Nucl. Data Tables **26**, 33 (1981).
[37] M. Lewenstein, Ph. Balcou, M. Y. Ivanov, A. L'Huillier, and P. B. Corkum, Phys. Rev. A **49**, 2117 (1994).
[38] C. A. Haworth *et al.*, Nat. Phys. **3**, 52 (2007).
[39] V. S. Yakovlev, M. Ivanov, and F. Krausz, Opt. Express **15**, 15351 (2007).
[40] A.-T. Le, R. R. Lucchese, S. Tonzani, T. Morishita, and C. D. Lin, Phys. Rev. A **80**, 013401 (2009).
[41] http://www.nist.gov/pml/data/asd.cfm.
[42] A. Leredde, A. Cassimi, X. Fléchard, D. Hennecart, H. Jouin, and B. Pons, Phys. Rev. A **85**, 032710 (2012).
[43] L. F. Errea *et al.*, J. Phys. B **32**, L673 (1999); **33**, 3107 (2000).
[44] R. Abrines and I. C. Percival, Proc. R. Soc. London **88**, 861 (1966).
[45] D. Eichenauer, N. Grun, and W. Scheid, J. Phys. B **14**, 3929 (1981).
[46] D. J. W. Hardie and R. E. Olson, J. Phys. B **16**, 1983 (1983).
[47] L. F. Errea *et al.*, Phys. Rev. A **70**, 052713 (2004).
[48] P. Botheron and B. Pons, Phys. Rev. A **80**, 023402 (2009).
[49] M. J. Raković, D. R. Schultz, P. C. Stancil, and R. K. Janev, J. Phys. A **34**, 4753 (2001).
[50] N. L. Balazs and A. Voros, Ann. Phys. (NY) **199**, 123 (1990).
[51] S. Keshavamurthy and W. H. Miller, Chem. Phys. Lett. **218**, 189 (1994).
[52] N. T. Maitra and E. J. Heller, Phys. Rev. Lett. **78**, 3035 (1997).
[53] H. Soifer, P. Botheron, D. Shafir, A. Diner, O. Raz, B.D. Bruner, Y. Mairesse, B. Pons, and N. Dudovich, Phys. Rev. Lett. **105**, 143904 (2010).
[54] G. Cerullo, A. Baltuška, O. D. Mücke, and C. Vozzi, Laser Photon. Rev. **5**, 323 (2011).
[55] M. V. Frolov, N. L. Manakov, T. S. Sarantseva, and A. F. Starace, J. Phys. B **42**, 035601 (2009).
[56] T. Morishita, A.-T. Le, Z. Chen, and C. D. Lin, Phys. Rev. Lett. **100**, 013903 (2008).
[57] M. V. Frolov, N. L. Manakov, T. S. Sarantseva, and A. F. Starace, Phys. Rev. A **86**, 063406 (2012).
[58] B. Schmidt, F. Légaré, and D. Villeneuve (private communication).
[59] http://www.mcia.univ-bordeaux.fr.